第 35 卷第 4 期
2019 年 4 月

无 机 化 学 学 报
CHINESE JOURNAL OF INORGANIC CHEMISTRY

Vol.35 No.4
711-719

PbF_2:Er^{3+},Yb^{3+}荧光粉的制备和多波长响应双向转换发光机理

马小易 李 彪 王一帆 胡 盼 严通廷 柏朝晖*
(长春理工大学材料科学与工程学院,长春 130022)

摘要: 采用高温固相法制备了 PbF_2:Er^{3+},Yb^{3+}双向转换荧光粉。通过 X 射线粉末衍射分析(XRD)、结构精修分析、功率–强度测试和荧光光谱分析对样品进行了表征。通过 X 射线衍射和精修结果分析了样品的相组成和晶胞参数的变化。荧光光谱分析表明,在紫外光(378 nm)和不同波长的红外光(808、980、1 064 和 1 550 nm)激发下,样品在 540~550 nm 范围内具有强绿光发射和在 650~660 nm 范围内的弱红光发射。最后,通过强度–功率测试讨论了样品在不同波长的红外光下激发的上转换发光机理,并分析了在 378 nm 激发的下转换发光机理。

关键词: 氟化铅; 高温固相法; Er^{3+}-Yb^{3+}掺杂; 双向转换发光; 多波长响应
中图分类号: O482.31 **文献标识码**: A **文章编号**: 1001-4861(2019)04-0711-09
DOI:10.11862/CJIC.2019.070

Preparation of PbF_2:Er^{3+},Yb^{3+} Phosphors and Multi-Wavelength Sensitive Bidirectional Conversion Luminescence Mechanism

MA Xiao-Yi LI Biao WANG Yi-Fan HU Pan YAN Tong-Ting BAI Zhao-Hui*
(*School of Materials Science and Engineering, Changchun University of Science and Technology, Changchun* 130022, *China*)

Abstract: PbF_2:Er^{3+},Yb^{3+} bidirectional conversion phosphors were successful prepared by the high temperature solid-state reaction method. The samples were characterized by X-ray powder diffraction (XRD), general structure analysis system structure refinement, the intensity-power test and fluorescence spectrum method. XRD and Rietveld refinement were performed to analyze the phase composition and the changes of cell parameters. The fluorescence spectra analysis showed the samples exhibited the intense green emissions in the range of 540~550 nm and weak red emission in the range of 650~660 nm when excited at ultraviolet (378 nm) and different infrared wavelengths (808, 980, 1 064 and 1 550 nm). Finally, luminescence mechanisms excited at different infrared wavelengths were discussed by means of the intensity-power test, and the down-conversion (DC) luminescence mechanism excited at 378 nm was analyzed.

Keywords: lead fluoride; high temperature solid-state method; Er^{3+}-Yb^{3+} co-doped; bidirectional conversion; multi-wavelength sensitive

0 Introduction

Over the past few decades, lanthanide-doped luminescence materials exhibited promising prospects for application in upconversion lasers[1-2], display technologies[3-4], medical treatment[5-6], anti-counterfeit technologies[7-8] and solar cells[9-10]. In particular, the application of up- and down-conversion phosphors to solar cells has attracted the attention of a large number of scientific researchers[11-12]. In past study, ultraviolet (UV) and infrared light conversion to visible light were realized by doping of different lanthanide ions in

收稿日期:2018-10-31。收修改稿日期:2019-01-15。
国家自然科学基金(No.51602027,61307118)、吉林省教育厅项目(No.JJKH20170607KJ)资助。
*通信联系人。E-mail:zhaohuibai@126.com

different materials [13-16]. Yu et al.[17] prepared Er^{3+}-Yb^{3+} co-doped $TiO_{2-x}F_x$ upconversion luminescence powder via hydrothermal method. They applied the upconversion-$TiO_{2-x}F_x$ into dye sensitized solar cell (DSSC) and obtained an overall energy conversion efficiency of 7.08%. Zhang et al.[18] prepared $SrAl_2O_4$:Eu^{2+},Dy^{3+} powder via a combustion method, spectral characterization showed that it can convert ultraviolet (200~400 nm) to visible luminescence (520 nm). The solar conversion efficiency for a DSSC with $SrAl_2O_4$:Eu^{2+},Dy^{3+} doping (weight ratio of phosphor powder to TiO_2 was 7∶100) reached 7.938%. However, research on the fluorescence properties of bidirectional conversion luminescent materials that simultaneously convert ultraviolet and infrared light into visible light have rarely been reported.

Compared with other matrix materials, such as oxysulfide and $NaYF_4$, lead fluoride (PbF_2) have the advantage of excellent fluorescence response under 1 064 and 1 550 nm excitation, and are a fair good host material for bidirectional conversion luminescence[19-20]. In this work, we reported a bidirectional conversion PbF_2:Er^{3+},Yb^{3+} phosphors, which could convert both UV light (378 nm) and infrared light (808, 980, 1 064 and 1 550 nm) into visible light (blue, green and red). Therefore, the as-prepared phosphors could improve conversion efficiency of solar cells and be widely used in solar cells. The bidirectional conversion PbF_2:Er^{3+},Yb^{3+} phosphors were synthesized by the high temperature solid-state reaction method. The luminescence properties of the phosphors were analyzed. In addition, the down-conversion (DC) and up-conversion (UC) multi-wavelength sensitive luminescence mechanisms of the samples were discussed in detail.

1 Experimental

1.1 Preparation

PbF_2:Er^{3+},Yb^{3+} bidirectional conversion phosphors were prepared via the high temperature solid-state reaction method. PbF_2 (99.99%), Na_2SiF_6 (99.99%) were purchased from Shanghai Sinopharm Chemical Reagent Company. Er_2O_3 (99.99%), YbF_3 (99.99%) were purchased from Hawei Ruike Chemical Reagent Company, HNO_3 (65%~68% (*w*/*w*)), HF (40% (*w*/*w*)) and anhydrous ethanol were purchased from Beijing Chemical Company. Firsly, excess diluted HNO_3 was added into the Er_2O_3 and stirred on a magnetic stirrer until the oxides were completely dissolved. After cooling, poured the mixed solution into a plastic cup and HF was added into the solution to obtain ErF_3 precipitates, and washed several times. Then, the molar ratio of PbF_2∶ErF_3∶YbF_3 was 80∶2∶18 according to the composition of the compound. Reactants were weighed according to a predetermined molar ratio and thoroughly ground in an agate mortar. Finally, the base materials were placed in a crucible covered with $NaSiF_6$, heated to predetermined temperature (650 ℃) under a fluoride atmosphere provided by the decomposition of $NaSiF_6$ and sintered for a certain time (1.5 h) to get the $(Pb_{0.80}Er_{0.02}Yb_{0.18})F_2$ phosphors.

1.2 Measurements

The XRD patterns were performed using a Rigaku D/max IIB diffractometer which recorded diffraction angel (2θ) from 20° to 80°, Cu $K\alpha_1$ (λ=0.154 06 nm) was used as the radiation source with an accelerating voltage of 40 kV and a working current of 20 mA. The structure refinement data was collected through using the general structure analysis system (GSAS) software. The emission spectra and the intensity-power curves were measured with UV-Vis spectrophotometry using RF-5301PC coupled 808, 980, 1 064 and 1 550 nm laser. All the measurement data were performed at room temperature.

2 Results and discussion

2.1 Phase identification and crystal structure

Fig.1(a) gives XRD pattern of the $(Pb_{0.80}Er_{0.02}Yb_{0.18})F_2$ phosphors. It is seen that all peak positions were consistent with the standard PDF No.06-0251 of cubic PbF_2. The XRD results indicated that the synthesized sample was a cubic PbF_2 structure with the space group of *Fm*3*m* (225). The Er^{3+} and Yb^{3+} ions have successfully entered PbF_2 host lattice by occupying the Pb^{2+} sites; there was no impurity phase, which demonstrated that the synthetic crystal was pure

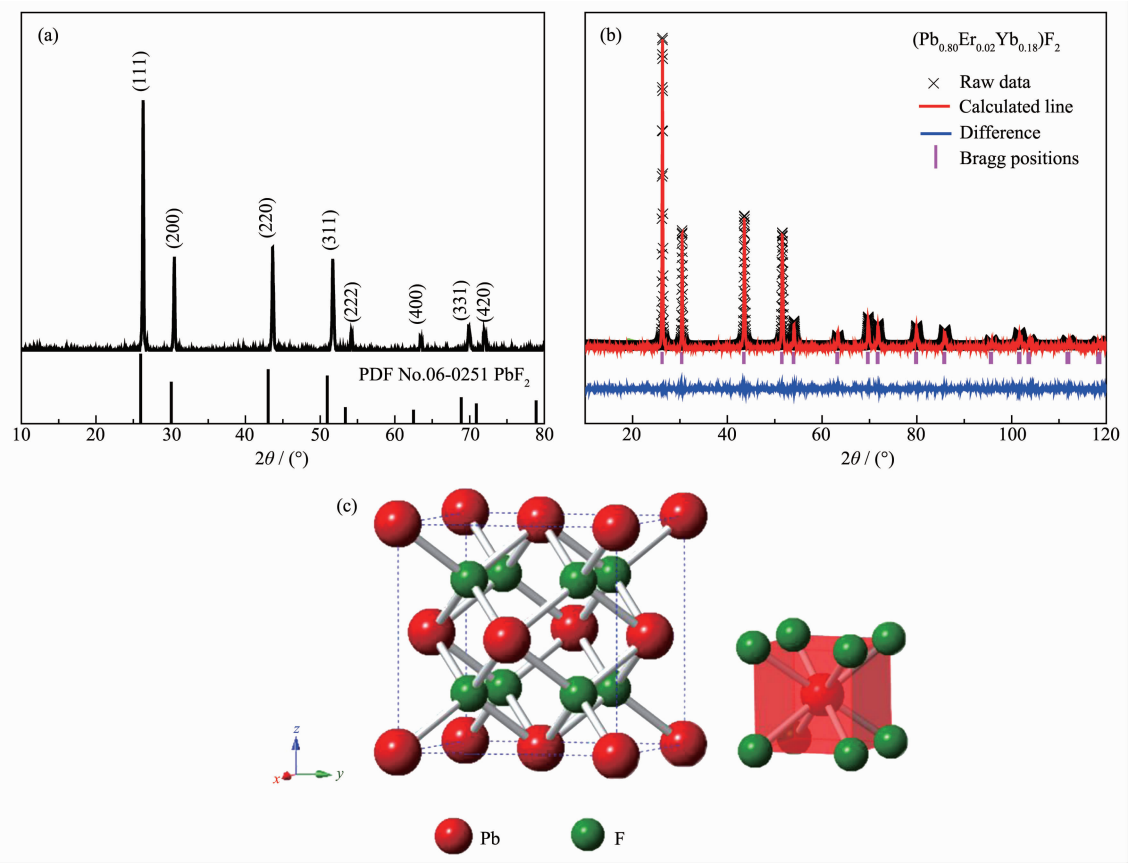

Fig.1　(a) XRD pattern of the $(Pb_{0.80}Er_{0.02}Yb_{0.18})F_2$ sample; (b) Rietveld refinement of the XRD pattern of $(Pb_{0.80}Er_{0.02}Yb_{0.18})F_2$ sample; (c) Crystal structure representation of PbF_2

phase. Fig.1(b) displays the refinement pattern of the $(Pb_{0.80}Er_{0.02}Yb_{0.18})F_2$ phosphor. The final refinement converged with indicator of goodness of fit χ^2=1.858, with weighted profile factor R_{wp}=9.63%, and with profile factor R_p=7.76%, The comparison between experimental and calculated results illustrated that sample could better crystallize in the cubic. Fig.1(c) gives the crystal structure of PbF_2 and 8 coordination of Pb^{2+}, which are distributed in face-centered cubic (FCC) crystal structure.

Table 1 presents the refinement result and structure parameter for $(Pb_{0.80}Er_{0.02}Yb_{0.18})F_2$ phosphors. According to the data acquired by refinement, the occupation ratio of the Er^{3+}/Yb^{3+} ions was 14.08% of the Pb^{2+} position, indicating that the doped Er^{3+}/Yb^{3+} ions could effectively enter the PbF_2 lattice cell. The lattice parameters are $a=b=c$=0.585 7 nm, $\alpha=\beta=\gamma$=90°. The crystal structure of resultant sample shifted to high angle in comparison with the peak positions of the standard PbF_2 crystallographic data (PDF No.06-0251, $a=b=c$=0.594 nm, $\alpha=\beta=\gamma$=90°), which was mainly cause via bigger radius (Pb^{2+}: 0.143 nm) replaced by smaller radius (Er^{3+}: 0.117 nm, Yb^{3+}: 0.113 nm).

The Er^{3+} and Yb^{3+} ions entered PbF_2 lattice to replace Pb^{2+} ions to form $Er_{Pb}^{\cdot}$ and $Yb_{Pb}^{\cdot}$ and F_F, and the F^- ions in ErF_3 and YbF_3 entered PbF_2 lattice to replace F^- ions to form F_F. The excess F^- ions entered $[F_8]$ interspace in unit cell, forming an interstitial F_i'. Because the valence of both Er^{3+} and Yb^{3+} ions are higher than that of Pb^{2+} ions, charge imbalance is produced. The imbalance of charge between replacement and substituted ions leads to formation of vacant ions or interstitial ions[21-22]. The possible reactions when Er^{3+} and Yb^{3+} ions entered into lattice sites of Pb^{2+} ions were displayed below:

$$ErF_3 \xrightarrow{PbF_2} Er_{Pb}^{\cdot}+2F_F+F_i' \quad (1)$$

$$YbF_3 \xrightarrow{PbF_2} Er_{Pb}^{\cdot}+2F_F+F_i' \quad (2)$$

The relative difference between the ionic radius of Er^{3+} and Yb^{3+} ions and the ionic radius of Pb^{2+} ions

Table 1 Refinement results and structure parameters for $(Pb_{0.80}Er_{0.02}Yb_{0.18})F_2$

Formula	$(Pb_{0.80}Er_{0.02}Yb_{0.18})F_2$
Crystal system	Cubic
Space group	*Fm*3*m* (225)
Z	4
a=*b*=*c* / nm	0.585 7
χ^2	1.858
R_p	7.76%
R_{wp}	9.63%

Atom	*X*	*Y*	*Z*	Occupation ratio
Pb1	0.000	0.000	0.000	0.859 2
Er^{3+}/Yb^{3+}	0.000	0.000	0.000	0.140 8
F1	0.250	0.250	0.250	1

is not more than 15%, which improves the tendency of replacement. More importantly, the presence of $[F_8]$ interspace in PbF_2 cell creates favorable conditions for the entry of F^- (0.133 nm) into the lattice either in size (the length of $[F_8]$ interspace is 0.297 nm) or energy, so that the interstitial ion is in well coordination with interspace position.

2.2 Luminescent properties under excitation of 378 nm

Fig.2 exhibits the emission and excitation spectrum of the optimal sample. Fig.2a shows the excitation spectrum of the $PbF_2:Er^{3+},Yb^{3+}$ sample at 550 nm, which could be excited from the UV to the visible region, and highest peak intensity of the excitation spectrum at 378 nm. Therefore, to obtain a higher DC efficiency, the DC luminescence property of $PbF_2:Er^{3+},Yb^{3+}$ system at 378 nm excitation was studied. Fig.2b presents the DC spectrum of the sample excited at 378 nm. It could be divided into three parts: (1) A blue emission band with an emission peak near 409 nm; (2) Both peaks are located at the green light emission band near 521 and 550 nm; (3) A red-light emission center around 650 nm. The emission peaks at ~409, ~521, ~550 and ~650 nm correspond to the $^2H_{9/2}\rightarrow{}^4I_{15/2}$, $^2H_{11/2}\rightarrow{}^4I_{15/2}$, $^4S_{3/2}\rightarrow{}^4I_{15/2}$ and $^4F_{9/2}\rightarrow{}^4I_{15/2}$ transitions, respectively.

Fig.3 describes the Yb^{3+}-Er^{3+} energy-level diagram of the sample excited at 378 nm. First, the electrons could be pumped from $^4I_{15/2}$ to $^4G_{11/2}$ by absorbing the energy of near-ultraviolet light at 378 nm, and Er^{3+} ions transfered part of the energy to Yb^{3+} ions, producing Yb^{3+}:$^2F_{5/2}\rightarrow{}^2F_{7/2}$ transition. Then, because of the narrow energy gap between the $^4G_{11/2}$ and $^2H_{9/2}$, the $^4G_{11/2}$ energy level in Er^{3+} could easily relax to the $^2H_{9/2}$ by

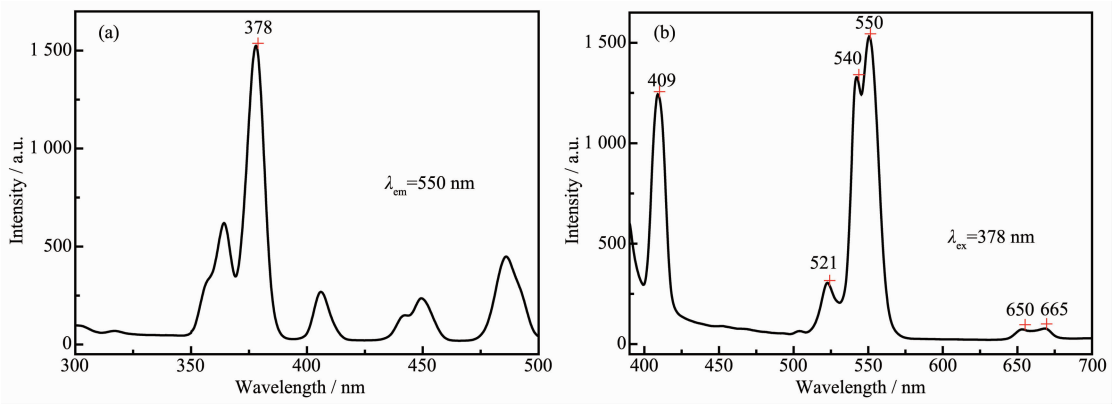

(a) λ_{em}=550 nm; (b) λ_{ex}=378 nm

Fig.2 Emission and excitation spectra of $(Pb_{0.80}Er_{0.02}Yb_{0.18})F_2$ sample

non-radiation relaxation. Subsequently, particles in $^2H_{9/2}$ returned to $^4I_{15/2}$ generating blue luminescence around 409 nm. At this time, Er^{3+} ions at the $^2H_{9/2}$ level might relax to the $^2H_{11/2}$, $^4S_{3/2}$, $^4F_{9/2}$ levels by the fast multiphoton process[23-24]. In the end, Er^{3+} ions decayed from $^2H_{11/2}$, $^4S_{3/2}$ and $^4F_{9/2}$ to the ground state $^4I_{15/2}$ and emitted 521, 550 and 650 nm red-green light emission, respectively.

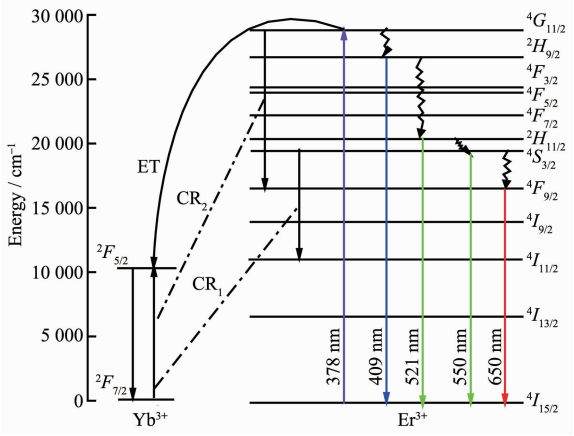

Fig.3　Er^{3+}-Yb^{3+} energy level diagram excited at 378 nm

The cross relaxation (CR_1) process results in particles significant reduction at the Er^{3+} ion $^4S_{3/2}$ level. Consequently, the emission intensity at 550 nm reduced. The CR_2 process leads to a significant increase in the population of the $^4F_{9/2}$ level of Er^{3+} ions. As a result, the 650 nm luminescence intensity was relatively enhanced.

$$CR_1: Er^{3+}(^4S_{3/2})+Yb^{3+}(^2F_{7/2}) \rightarrow Er^{3+}(^4I_{11/2})+Yb^{3+}(^2F_{5/2}) \quad (3)$$

$$CR_2: Er^{3+}(^4G_{11/2})+Yb^{3+}(^2F_{7/2}) \rightarrow Er^{3+}(^4F_{9/2})+Yb^{3+}(^2F_{5/2}) \quad (4)$$

2.3　Upconversion spectral analysis

Fig.4 depicts a series of UC emission spectra of optimal sample excited by different wavelength infrared light. Under excitation of 1 064, 980 and 808 nm lasers respectively, the spectra were presented an intense green emission at 540~550 nm as the result of the $^4S_{3/2} \rightarrow {}^4I_{15/2}$ transition of Er^{3+} ions, the weak green emission at 521 nm derived from the $^2H_{11/2} \rightarrow {}^4I_{15/2}$ transition while the weak red emission at 650~665 nm

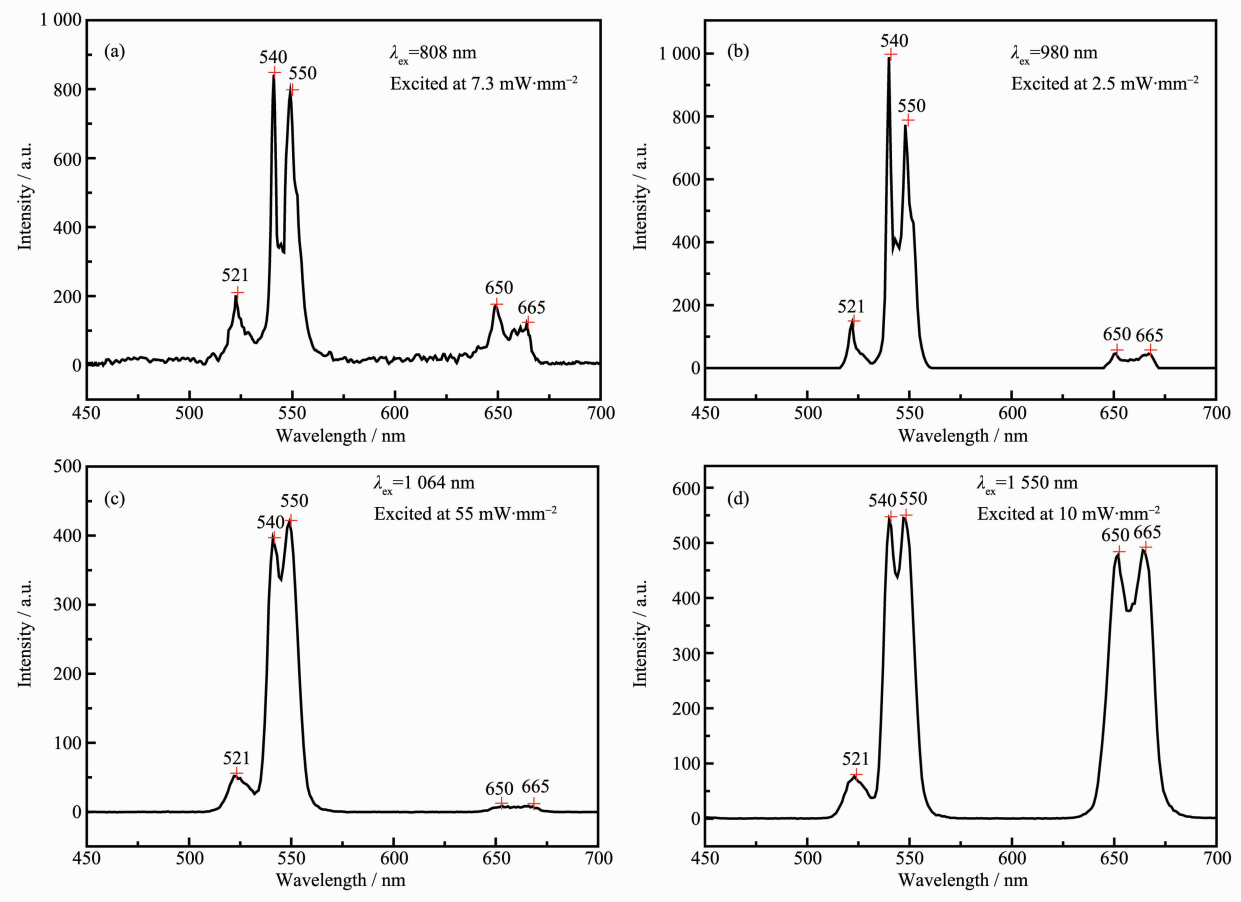

(a) 808, (b) 980, (c) 1 064 and (d) 1 550 nm

Fig.4　Emission spectra of the $(Pb_{0.80}Er_{0.02}Yb_{0.18})F_2$ excited at different wavelengths

originated from the $^4F_{9/2} \rightarrow {}^4I_{15/2}$ transition. Compared with other luminescence emission spectra, the phosphor presented an intense red emission under 1 550 nm excitation.

2.3.1 Luminescent mechanism analysis under 1 064 nm excitation

It is known that the emission spectrum of the trivalent rear earth (RE) ions doped UC material varies with excitation power[25]. To identify the relative mechanism of the three UC emissions of Er^{3+} ions excited at 1 064 nm at room temperature for the $(Pb_{0.80}Er_{0.02}Yb_{0.18})F_2$ sample. The dependence of emission intensities versus pump power is presented in Fig.5. The result is illustrated in the intensity-power plots, and the values of slopes for the ~521 nm (green), ~550 nm (green) and ~650 nm (red) were approximately to 2, indicating that the two-photon process was mainly responsible for the observed UC emission under 1 064 nm excitation.

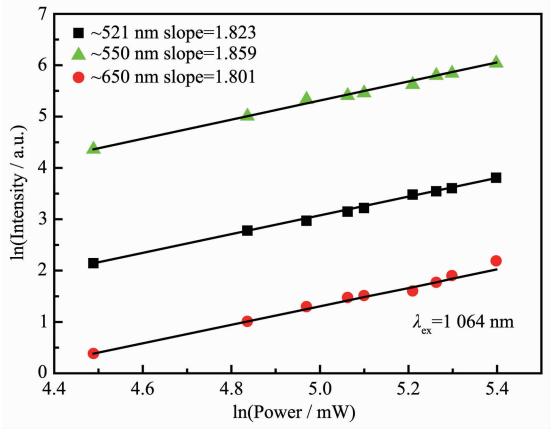

Fig.5 Intensity-power plots of the green and red emissions versus excitation power at 1064 nm

Fig.6 illustrates the simplified Er^{3+}-Yb^{3+} energy level diagram of sample under excitation of 1 064 nm. Er^{3+} ion acted as an activator and was the luminescent center of the sample. It is observed that the $^2F_{5/2}$ state of Yb^{3+} ions was very close to the $^4I_{11/2}$ state of Er^{3+} ions, therefore, an effective energy transmission process could take place between Er^{3+} and Yb^{3+} ions. Firstly, the $^2F_{5/2}$ state of Yb^{3+} ions could be populated through absorbing 1 064 nm infrared light. And the Er^{3+} ion transited from $^4I_{15/2}$ to $^4I_{11/2}$ level by ground state absorption (GSA) and energy transfer (ET_1) from Yb^{3+}

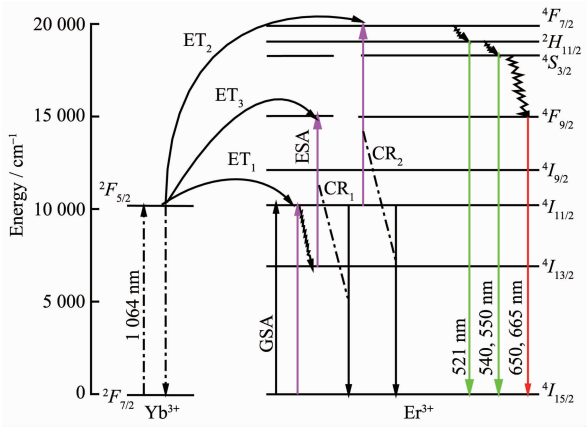

Fig.6 Er^{3+}-Yb^{3+} energy level diagram excited at 1 064 nm

ions. Then, the electrons could be pumped from $^4I_{11/2}$ state of Er^{3+} ions to $^4F_{7/2}$ state through ET_2 process:

GSA: $Er^{3+}(^4I_{15/2})$+a 1 064 nm photon $\rightarrow Er^{3+}(^4I_{11/2})$ (**5**)

ET_1: $Er^{3+}(^4I_{15/2})+Yb^{3+}(^2F_{5/2}) \rightarrow Er^{3+}(^4I_{11/2})+Yb^{3+}(^2F_{7/2})$ (**6**)

ET_2: $Er^{3+}(^4I_{11/2})+Yb^{3+}(^2F_{5/2}) \rightarrow Er^{3+}(^4F_{7/2})+Yb^{3+}(^2F_{7/2})$ (**7**)

Furthermore, Er^{3+} ions at the $^4F_{7/2}$ level might relax to the $^2H_{11/2}$ and $^4S_{3/2}$ levels by the fast-multiphoton process. Subsequently, Er^{3+} ions at the $^2H_{11/2}$ and $^4S_{3/2}$ energy level returned to the ground state $^4I_{15/2}$ while emitting green light at 521 and 550 nm, respectively. In addition, Er^{3+} ions at the $^4I_{11/2}$ level possibly underwent a non-radiative transition to reach the $^4I_{13/2}$ levels, and the Er^{3+} ion transited from the excited state $^4I_{13/2}$ to $^4F_{9/2}$ level by excited state absorption (ESA) and ET_3:

ESA: $Er^{3+}(^4I_{13/2})$+a 1 064 nm photon $\rightarrow Er^{3+}(^4F_{9/2})$ (**8**)

ET_3: $Er^{3+}(^4I_{13/2})+Yb^{3+}(^2F_{5/2}) \rightarrow Er^{3+}(^4F_{9/2})+Yb^{3+}(^2F_{7/2})$ (**9**)

Finally, the electron at the $^4F_{9/2}$ level returns to $^4I_{15/2}$ ground state and emitted weak red fluorescence at 650 nm. Furthermore, the CR_1 and CR_2 process among Er^{3+} ions enhanced the UC luminescence efficiency of the sample[26]:

CR_1: $Er^{3+}(^4I_{13/2})+Er^{3+}(^4I_{11/2}) \rightarrow Er^{3+}(^4F_{9/2})+Er^{3+}(^4I_{15/2})$ (**10**)

CR_2: $Er^{3+}(^4I_{11/2})+Er^{3+}(^4I_{11/2}) \rightarrow Er^{3+}(^4F_{7/2})+Er^{3+}(^4I_{15/2})$ (**11**)

2.3.2 Luminescent mechanism analysis under 1 550 nm excitation

Fig.7 depicts the measured power dependence of the three UC emissions of Er^{3+} ions excited by 1 550 nm at room temperature for the $(Pb_{0.80}Er_{0.02}Yb_{0.18})F_2$ sample. The result is illustrated in the intensity-power plots, the green and red emissions exhibited a sub-cubic (2.675, 2.60 and 2.873) power-law behavior for

the excitation at 1 550 nm, which indicated that three pumping photons around 1 550 nm participate in the UC excitation process.

Fig.8 presents the energy-level diagram of the sample excited by 1 550 nm. Yb^{3+} ions could not absorb 1 550 nm infrared light, hence the UC luminescence should depend on the absorption process of Er^{3+} ions and the energy transfer up-conversion (ETU) process among Er^{3+} ions. When excited by 1 550 nm infrared light, Er^{3+} ions were promoted from the ground state $^4I_{15/2}$ to the first excited state $^4I_{13/2}$ by GSA. Subsequently, the Er^{3+} ion transited from the excited state $^4I_{13/2}$ to $^4I_{9/2}$ level by ESA_1 and ETU_1[27-28]:

GSA: $Er^{3+}(^4I_{15/2})$+a 1 550 nm photon → $Er^{3+}(^4I_{13/2})$ (**12**)

ESA_1: $Er^{3+}(^4I_{13/2})$+a 1 550 nm photon → $Er^{3+}(^4I_{9/2})$ (**13**)

ETU_1: $Er^{3+}(^4I_{13/2})+Er^{3+}(^4I_{13/2})$ → $Er^{3+}(^4I_{11/2})+Er^{3+}(^4I_{15/2})$ (**14**)

Then, the electrons at $^4I_{9/2}$ state could transit to $^2H_{11/2}$ state through ESA_2 and transit to $^4I_{11/2}$ level by the no-radiation relaxation process, and through the ETU_2 process transitions to the higher excited state $^2H_{11/2}$:

ESA_2: $Er^{3+}(^4I_{9/2})$+a 1 550 nm photon → $Er^{3+}(^2H_{11/2})$ (**15**)

ETU_2: $Er^{3+}(^4I_{13/2})+Er^{3+}(^4I_{9/2})$ → $Er^{3+}(^4I_{15/2})+Er^{3+}(^2H_{11/2})$ (**16**)

Finally, the Er^{3+}ions at the $^2H_{11/2}$ state relaxed to the $^4S_{3/2}$ and $^4F_{9/2}$ level by the fast-multiphoton process. The radiation decayed from the $^2H_{11/2}$,$^4S_{3/2}$ and $^4F_{9/2}$ states to the ground state and generated UC luminescence at 521, 540~550 nm and 650~665 nm, respectively.

Compared with other luminescence emission spectra, the red emission of the sample under 1 550 nm excitation was increased. The increase of the red component in the sample was mainly due to the ETU_3 between the Er^{3+} ion at the $^4I_{13/2}$ and $^4I_{11/2}$ level[29-30], resulting in an increase of Er^{3+} ions at the $^4F_{9/2}$ level.

ETU_3: $Er^{3+}(^4I_{13/2})+Er^{3+}(^4I_{11/2})$ → $Er^{3+}(^4I_{15/2})+Er^{3+}(^4F_{9/2})$ (**17**)

2.3.3 Luminescent mechanism analysis under 980 nm excitation

The dependence excited by 980 nm is illustrated in the intensity-power plots in Fig.9. The green and red emissions exhibited a sub-square power-law behavior for the excitation at 980 nm, the values of slopes for the ~521 nm green emission, ~550 nm green emission and ~650 nm red emission are 1.857, 1.920 and 1.831, respectively. It is suggested that two pumping photons around 980 nm participate in the UC excitation process.

Fig.10 describes the simplified Yb^{3+}-Er^{3+} energy-

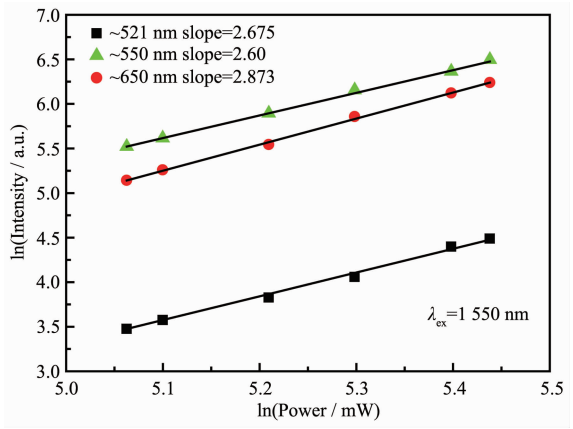

Fig.7　Intensity-power plots of the green and red emissions versus excitation power at 1 550 nm

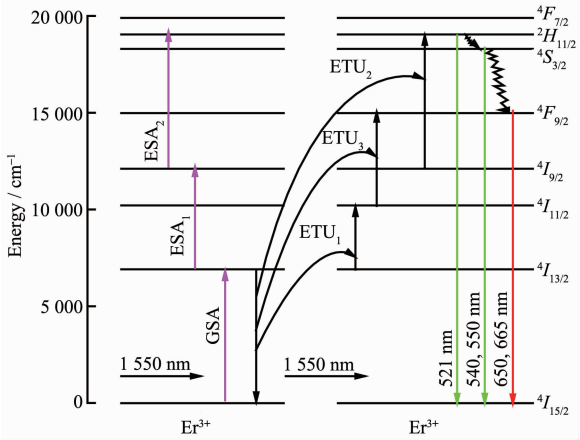

Fig.8　Er^{3+}-Yb^{3+} energy level diagram excited at 1 550 nm

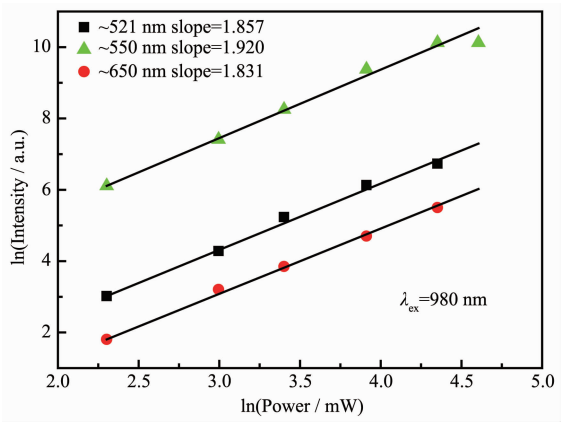

Fig.9　Intensity-power plots of the green and red emissions versus excitation power at 980 nm

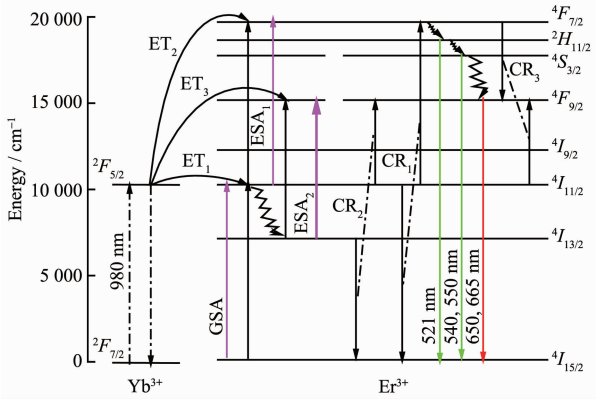

Fig.10 Er^{3+}-Yb^{3+} energy level diagram excited at 980 nm

level diagram of the sample under excitation of 980 nm. First, when the sample was irradiated by 980 nm laser, Yb^{3+} ions transited from the ground state $^2F_{7/2}$ to $^2F_{5/2}$ level. Then, the Er^{3+} ion transited from the ground state to $^4I_{11/2}$ was through either GSA or ET_1 process between Yb^{3+} and Er^{3+} ions:

GSA: $Er^{3+}(^4I_{15/2})$+a 980 nm photon → $Er^{3+}(^4I_{11/2})$ **(18)**

ET_1: $Er^{3+}(^4I_{15/2})+Yb^{3+}(^2F_{5/2}) \rightarrow Er^{3+}(^4I_{11/2})+Yb^{3+}(F_{7/2})$ **(19)**

Similarly, the Er^{3+} ion transited from the excited state $^4I_{11/2}$ to $^4F_{7/2}$ level by ESA_1, CR_1, ET_2:

ESA_1: $Er^{3+}(^4I_{11/2})$+a 980 nm photon → $Er^{3+}(^4F_{7/2})$ **(20)**

ET_2: $Er^{3+}(^4I_{11/2})+Yb^{3+}(^2F_{5/2}) \rightarrow Er^{3+}(^4F_{7/2})+Yb^{3+}(^2F_{7/2})$ **(21)**

CR_1: $Er^{3+}(^4I_{11/2})+Er^{3+}(^4I_{11/2}) \rightarrow Er^{3+}(^4I_{15/2})+Er^{3+}(^4F_{7/2})$ **(22)**

In addition, Er^{3+} ions at the $^4F_{7/2}$ level relaxed to the $^2H_{11/2}$ and $^4S_{3/2}$ levels by the fast-multiphoton process. Then, the radiation decayed from the $^2H_{11/2}$ and $^4S_{3/2}$ levels to the $^4I_{15/2}$ ground state and generated green UC emission at 521 and 550 nm, respectively. Red UC emission mainly came from the population of $^4F_{9/2}$ level of Er^{3+} ions[31-32]. The Er^{3+} ions at $^4I_{11/2}$ relaxed to the $^4I_{13/2}$ by the fast-multiphoton process and then transit to $^4F_{9/2}$ level by ESA_2, CR_2, CR_3 and ET_3:

ESA_2: $Er^{3+}(^4I_{13/2})$+a 980 nm photon → $Er^{3+}(^4F_{9/2})$ **(23)**

CR_2: $Er^{3+}(^4I_{13/2})+Er^{3+}(^4I_{11/2}) \rightarrow Er^{3+}(^4I_{15/2})+Er^{3+}(^4F_{9/2})$ **(24)**

CR_3: $Er^{3+}(^4F_{7/2})+Er^{3+}(^4I_{11/2}) \rightarrow Er^{3+}(^4F_{9/2})+Er^{3+}(^4F_{9/2})$ **(25)**

ET_3: $Er^{3+}(^4I_{13/2})+Yb^{3+}(^2F_{5/2}) \rightarrow Er^{3+}(^4F_{9/2})+Yb^{3+}(^2F_{7/2})$ **(26)**

Finally, the electronic at $^4F_{9/2}$ level decayed to $^4I_{15/2}$ ground state and emitted red fluorescence at 650 nm. In summary, the red UC luminescence intensity was not as strong as the green emission, which was due to the large energy gap between the $^4S_{3/2}$ and $^4F_{9/2}$ energy levels, making it difficult to relax without radiation.

2.3.4 Luminescent mechanism analysis under 808 nm excitation

Fig.11 presents the energy-level diagram of the sample excited at 808 nm. Firstly, Er^{3+} ions are promoted from $^4I_{15/2}$ to $^4I_{9/2}$ by absorb an 808 nm photon (GSA). Since $^4I_{9/2}$, $^4I_{11/2}$ and $^4I_{13/2}$ belonged to different spectral branches of the same spectral term, Er^{3+} ions at the $^4F_{9/2}$ level relaxed to the $^4I_{11/2}$ and $^4I_{13/2}$ levels by no-radiation transitions process. Subsequently, the Er^{3+} ions at $^4I_{13/2}$ could absorb an 808 nm photon to transit to $^4F_{7/2}$ and $^4S_{3/2}$ level (ESA_1, ESA_2). Then, the radiation decayed from the $^4S_{3/2}$ levels to the $^4I_{15/2}$ and generated green UC emission 550 nm. In addition, the CR_2 phenomenon caused energy transfer between ions at the $^4I_{11/2}$ level, Er^{3+} ions at the $^4F_{7/2}$ level might relax to $^2H_{11/2}$ by the fast-multiphoton process, the radiation decayed from the $^2H_{11/2}$ levels to the $^4I_{15/2}$ generateed weak green UC emission at 521 nm. Finally, another CR_1 between $^4I_{11/2}$ and $^4I_{13/2}$ level resulted in a large accumulation of ions at the $^4F_{9/2}$ level, the electronic at $^4F_{9/2}$ level decayed to $^4I_{15/2}$ and emitted red fluorescence at 650 nm[33].

CR_1: $Er^{3+}(^4I_{13/2})+Er^{3+}(^4I_{11/2}) \rightarrow Er^{3+}(^4F_{9/2})+Er^{3+}(^4I_{15/2})$ **(27)**

CR_2: $Er^{3+}(^4F_{11/2})+Er^{3+}(^4I_{11/2}) \rightarrow Er^{3+}(^4F_{7/2})+Er^{3+}(^4F_{15/2})$ **(28)**

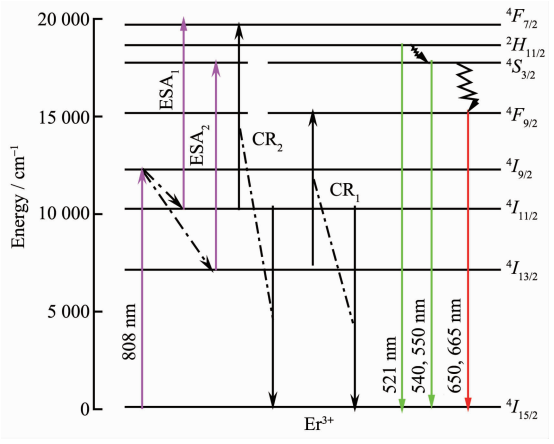

Fig.11 Er^{3+}-Yb^{3+} energy level diagram excited at 808 nm

3 Conclusions

In summary, we report on the bidirectional conversion properties of Er^{3+}-Yb^{3+} co-doped PbF_2 prepared by high temperature solid-state reaction method,

which may be used for enhancement of the conversion efficiency of solar cells. XRD and structure refinement data showed the Er^{3+}/Yb^{3+} occupied solely Pb^{2+} sites in the crystal host. Through analysis the DC and UC multi-wavelength sensitive luminescence mechanisms of the phosphor, it is found that the resultant phosphor could simultaneously convert both UV light (378 nm) and infrared light (808, 980, 1 064 and 1 550 nm) into visible light (blue, green and red) which could improve conversion efficiency of solar cells.

Acknowledgments: This project is financially supported by the National Natural Science Foundation of China (Grant No. 51602027 and 61307118), the Education Project of Jilin Provincial Department, China (Grant No.JJKH20170607KJ).

Compliance with ethical standards: Conflict of interest: The authors declare that they have no conflict of interest.

References:

[1] Cheng Y Y, Fuckel B, Khoury T, et al. *Energy Environ. Sci.*, **2012**,**5**(5):6953-6959

[2] Yuan C Z, Chen G Y, Li L, et al. *ACS Appl. Mater. Interfaces.*, **2014**,**6**(20):18018-18025

[3] Cho J Y, Ko K Y, Do Y R. *Thin Solid Films.*, **2007**,**515**(7): 3373-3379

[4] Rapaport A, Milliez J, Bass M, et al. *J. Disp. Technol.*, **2006**, **2**(1):68-78

[5] Chen G Y, Liu Y, Zhang Y G, et al. *Appl. Phys. Lett.*, **2007**, **91**(13):133103

[6] Wang G F, Peng Q, Li Y D. *J. Am. Chem. Soc.*, **2009**,**131** (40):14200-14201

[7] ZHANG Xiao-qing(张小青), LIN Xiang(林祥), QIAO Xu-Sheng(乔旭升) *J. Mater. Sci. Eng.*(材料科学与工程学报), **2010**,**28**(5):663-666

[8] You M L, Zhong J J, Hong Y, et al. *Nanoscale.*, **2015**,**7**(10): 4423-4431

[9] Yuan C Z, Chen G Y, Prasad P N, et al. *J. Mater. Chem.*, **2012**,**22**(33):16709-16713

[10]Ramasamy P, Manivasakan P, Kim J. *RSC Adv.*, **2014**,**4** (66):34873-34895

[11]Shockley W, Queisser H J. *J. Appl. Phys.*, **1961**,**32**(3):510-519

[12]Yella A, Lee H W, Tsao H N, et al. *Science.*, **2011**,**334** (6056):629-634

[13]Hirai T, Orikoshi T. *J. Colloid Interface Sci.*, **2004**,**273**(2): 470-477

[14]Hosseini Z, Taghavinia N, Duang E W. *Mater. Lett.*, **2016**,**188** (104):92-94

[15]Kumar G A, Pokhrel M, Sardar D K. *Mater. Lett.*, **2012**,**68** (1):395-398

[16]Kumar P, Kanika, Singh S, et al. *J. Lumin.*, **2017**,**196**(12): 207-213

[17]Yu J, Yang Y L, Fan R Q, et al. *J. Power Sources.*, **2013**, **243**:436-443

[18]Zhang J F, Lin J M, Wu J, et al. *J. Mater. Sci.-Mater. Electron.*, **2016**,**27**(2):1350-1356

[19]Wang H Q, Batentschuk M, Osvet A, et al. *Adv. Mater.*, **2011**,**23**(22/23):2675-2680

[20]Ma W, Yu W S, Dong X T, et al. *Chem. Eng. J.*, **2014**,**244** (7):531-539

[21]Lorbeer C, Behrends F, Cybinska J, et al. *J. Mater. Chem. C*, **2014**,**2**(44):9439-9450

[22]Sinha S, Mahata M K, Swart H C, et al. *New J. Chem.*, **2017**, **41**(13):5362-5372

[23]Luo X X, Cao W H. *Sci. China Chem.*, **2017**,**50**(4):505-513

[24]Xiao S, Yang X, Ding J W. *Appl. Phys. B*, **2010**,**99**(4):769-773

[25]Luo W J, Wang Y G, Chen Y P, et al. *J. Mater. Chem. C*, **2013**,**1**(36):5711-5717

[26]QIAN Jing-Xian(钱静娴), BAI Zhao-Hui(柏朝晖), ZHANG Xi-Yan(张希艳). *Journal of the Chinese Ceramic Society*(硅酸盐学报), **2013**,**41**(12):1725-1729

[27]BAI Zhao-Hui(柏朝晖), LI Xiu-Xian(李秀贤), ZHANG Xi-Yan(张希艳), et al. *Chinese J. Inorg. Chem.*(无机化学学报), **2012**,**28**(4):674-678

[28]Fan W, Zhang X Y, Chen L X, et al. *CrystEngComm*, **2015**, **17**(8):1881-1889

[29]ZHOU He-Feng(周禾丰), ZHANG Shu-Quan(张树全), WANG Hua(王华), et al. *Spectrosc. Spectr. Anal.*(光谱学与光谱分析), **2013**,**33**(1):23-26

[30]Tai Y, Wang H Y, Wang H, et al. *RSC Adv.*, **2015**,**6**(5): 4085-4089

[31]Georgobiani A N, Bogatyreva A A, Ishchenko V M, et al. *Inorg. Mater.*, **2007**,**43**(10):1073-1079

[32]YANG Kui-Sheng(杨魁胜), ZHAI Hai-Qing(翟海青), CUI Guang(崔光), et al. *Chinese J. Inorg. Chem.*(无机化学学报), **2009**,**25**(5):855-859

[33]Tian L J, Zheng X, Zhao S L, et al. *Materials*, **2014**,**7**(11): 7289-7303